Chemical Engineering Journal 387 (2020) 124161

Contents lists available at ScienceDirect

Chemical Engineering Journal

journal homepage: www.elsevier.com/locate/cej

Porous carbon prepared via combustion and acid treatment as flexible zinc-ion capacitor electrode material

Yiwei Zheng[a,b,1], Wei Zhao[b,1], Dedong Jia[b], Yue Liu[a,*], Liang Cui[a], Di Wei[a], Rongkun Zheng[a], Jingquan Liu[a,b,*]

[a] College of Materials Science and Engineering, Linyi University, Linyi, Shandong, China
[b] College of Materials Science and Engineering, Institute for Graphene Applied Technology Innovation, Collaborative Innovation Center for Marine Biomass Fibers Materials and Textiles of Shandong Province, Qingdao University, Qingdao 266071, China

HIGHLIGHTS

- Oxygen-enriched porous carbon (OPC) is rationally designed as electrode material.
- Gelatin gel is applied as electrolyte for zinc-ion hybrid capacitor (ZIC).
- The assembled capacitor displays high specific capacitance of 132.7 mA h g^{-1}.
- The assembled solid-state ZIC is flexible enough to withstand various deformations.
- The electrochemical kinetic of OPC electrode in ZIC is analyzed.

GRAPHICAL ABSTRACT

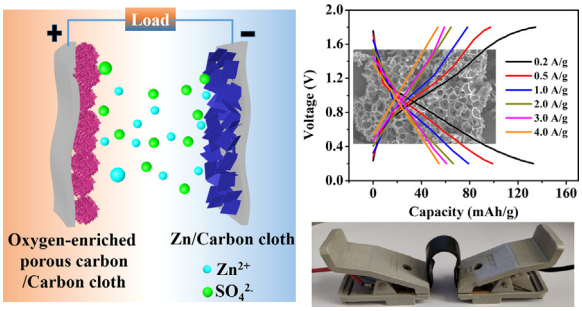

ARTICLE INFO

Keywords:
Oxygen-enriched porous carbon
Zn nanosheets
Zinc-ion capacitor
Flexible energy device

ABSTRACT

To meet the requirements for high energy/power density, safety and flexibility of wearable electronic devices simultaneously, a solid-state zinc-ion capacitor (ZIC) is assembled by integrating zinc nanosheets anode and porous carbon cathode with gelatin gel as electrolyte. Herein, the oxygen-enriched three-dimensional porous carbon has been synthesized as cathode of ZIC via a facile combustion and sequential acid-treatment process. Taking advantages of the rich oxygen-containing functional groups to provide pseudocapacitance and the specific pore structure of porous carbon to endow fast electrochemical kinetics of cathode, the assembled ZIC could deliver the superb specific capacity of 132.7 mA h g^{-1}, excellent energy density of 82.36 W h kg^{-1} and superior cycling stability with 87.6% capacity retention over 10,000 cycles at a current density of 1.0 A g^{-1}. Impressively, the assembled solid-state ZIC based on OPC is flexible enough to withstand various deformations including bending and twisting at large angles, which are promising to be applied in portable electronics.

1. Introduction

Nowadays, the increasing demand for portable and wearable electronics such as smart clothes, portable laptops, bendable displays and mobile phones has been inspiring the development of energy storage devices with high energy density, superior physical flexibility as well as good safety that are adaptable to the wearable applications [1,2]. Among various devices, rechargeable batteries have been widely investigated due to their high energy densities based on the charge storage mechanism in which cations (Li^+ or H^+) intercalate/de-

* Corresponding authors at: College of Materials Science and Engineering, Linyi University, Linyi, Shandong, China.
E-mail addresses: lyliuyue1990@gmail.com (Y. Liu), jliu@qdu.edu.cn (J. Liu).
[1] These authors contributed equally to this work.

https://doi.org/10.1016/j.cej.2020.124161
Received 20 September 2019; Received in revised form 3 December 2019; Accepted 17 January 2020
Available online 20 January 2020
1385-8947/

intercalate within the crystalline of electrode materials [3]. However, the intrinsic drawbacks of batteries including low power density and inferior security severely limit their broad practical applications for wearable electronics [4]. In contrast, supercapacitors (SCs) can provide much higher power densities, faster rate capabilities and longer cycle lifetimes, but the relatively low energy-to-power ratios restrict their further practical application in hybrid electrical vehicles [5]. Hence, a key target for a promising electrical energy storage device is to deliver both the high energy and high power at the same time in a single system.

Upon the combination of the rechargeable battery and SCs, hybrid capacitors with high energy density and fast charging rate, such as lithium-ion hybrid capacitors, potassium ion hybrid capacitors and sodium-ion hybrid capacitors have been achieved in recent years [6–8]. Normally these hybrid capacitor-type systems combine a battery-type electrode as anode to provide high energy density and a capacitor-type electrode as cathode to ensure high power density by the adsorption/desorption of univalent Li^+, Na^+ and K^+ [9]. However, the utilization of flammable organic electrolytes carries safety risks and makes them hard to be applied in flexible capacitors.

Metallic Zn, with a theoretical capacitance as high as 823 mA h g^{-1} and a low redox potential of -0.76 V, has been considered as a promising electrode material due to its better safety, lower cost and long-term cycling stability in neutral or slightly acidic electrolytes compared to reactive alkali metals [10–13]. Up to now, diverse kinds of rechargeable Zn ion energy storage devices have been widely investigated, such as “air chargeable” zinc-ion capacitor [14], manganese-based zinc ion battery [15], Zn-air batteries [16]. Based on the above advantages of Zn electrodes, Kang’s group reported a novel energy storage system of zinc-ion capacitors (ZICs) with Zn metal as anode, commercial activated carbon as cathode and $ZnSO_4$ aqueous solution as electrolyte, whose specific capacity could reach 121 mA h g^{-1} in a wide voltage range of 0.2–1.8 V and also deliver a high energy density of 84 Wh kg^{-1} [17]. Furthermore, they could utilize different AC materials to assemble AC//Zn ZICs and draw a conclusion that the high specific surface area of AC materials is beneficial for improving the specific capacity of ZICs devices. Very recently, Wang’ group reviewed the recent progresses in the research of multivalent metal ion hybrid capacitors (*e.g.,* zinc-ion hybrid capacitors, magnesium-ion hybrid capacitors, aluminum-ion hybrid capacitors and calcium-ion hybrid capacitors) [18]. They comprehensively elaborated the design concept, energy storage mechanism and electrochemical performance of multivalent metal ion hybrid capacitors. Those results make it extremely attractive for researchers to develop flexible solid-state zinc-ion capacitors. To the best of our knowledge, there have been only few studies focusing on the design of novel carbon cathode materials for flexible solid-state Zn-ions hybrid capacitors.

As a traditional method, high-temperature carbonization followed by KOH activation is an efficient way to improve the capacitance performance of carbon material. Herein, a combustion approach was used for the bottom-up synthesis of three-dimensional (3D) porous carbon materials (PC), in which sodium and ethanol reacted under a solvothermal condition to obtain a metastable solid that is easy to ignite. Interestingly, the obtained 3D carbon is O-doped as a result of the introduction of oxygen-containing functional groups onto the surface of carbon sheets. According to our previous work, treatment of unstable or fragile parts of carbon materials with concentrated acid at room temperature could effectively introduce oxygen-containing functional groups and increase specific surface area [19]. Thus, after immersing aforementioned combustion products into concentrated nitric acid, oxygen-enriched 3D porous carbon (OPC) was obtained and its applicability as cathode for Zn-ion hybrid supercapacitor was investigated. Owning to the porous and interconnected structure of the 3D carbon which endows the fast ion/electron transport and the abundant oxygen-containing functional groups for enhanced pseudocapacitance, the flexible solid-state ZIC not only achieves an excellent capacitance performance in terms of a high capacity of 132.7 mA h g^{-1}, a high energy density of 82.36 Wh kg^{-1} and power density of 3760 W kg^{-1}, but also could be bent at different angles without obvious diminution of capacitance.

2. Experimental

2.1. Synthesis of oxygen-enriched porous carbon samples

In a typical synthesis, 2 g sodium and 5 mL ethanol (at a molar ratio of 1:1) were added sequentially into a stainless-steel reactor with a maximum volume of 50 mL and then heated at 220 °C for 48 h to yield a white block product, which was then ground into powder and ignited. After the fire was naturally extinguished, the residue was transferred into a 250 mL beaker with 100 mL of deionized (DI) water and ultrasonically stirred for 1 h. The suspended solution was then vacuum filtered, washed with DI water for several times, and finally dried at 60 °C to afford the 3D porous carbon (PC).

100 mg of the obtained PC was added into a 25 mL beaker, followed by the slow addition of 6 mL concentrated nitric acid at room temperature. After soaking the PC in the concentrated acid for 3 h, the oxygen-enriched porous carbon (abbreviated as OPC) was collected by filtrating the above suspension, washing with DI water for several times until the pH reached neutral and then freeze drying.

2.2. Synthesis of Zn nanosheets deposited on carbon cloth

Firstly, commercial carbon cloth was washed with acetone and DI water in sequence to remove dirt. Before electrochemical activation, large-area cleaned carbon cloth was cut into strips (1 cm × 3 cm). Then, carbon cloth strips were electrochemically oxidized utilizing a standard three-electrode system in a mixed acid of HNO_3 and H_2SO_4 (volume ratio = 1) at a constant voltage of 3 V for 180 s, in which a platinum plate was used as counter electrode and saturated calomel electrode (SCE) as reference electrode. Finally, the acid-treated CC trips were washed with DI water for several times and dried at 80 °C.

The electrodeposition of Zn nanoflakes was carried out at a constant current of -40 mA cm^{-2} for 600 s in a three-electrode system in which acid-treated carbon cloth, SCE and platinum plate were used as working, reference and counter electrodes, respectively. The aqueous electrolyte for electrodeposition was prepared by dissolving 12.5 of zinc sulfate, 2.0 g of boric acid and 12.5 g of sodium sulfate in 100 mL of DI water. The mass loading of Zn anode is ~5 mg cm^{-2}.

2.3. Synthesis of the gel electrolyte

Gelatin gel electrolyte used in this work was prepared by mixing gelatin solution with dilute glutaraldehyde solution (1%). In specific, 3 g gelatin was added into the 30 mL $ZnSO_4$ aqueous solution (1 M) and stirred magnetically for 1 h, followed by boiling on an oil bath at 80 °C for 2 h. After cooling down to ambient temperature, the obtained gelatin/$ZnSO_4$ solution was dropped on the electrode materials. Finally, a small amount of dilute glutaraldehyde solution (1%) was brush-painted over the gelatin to get glutaraldehyde cross-linked gelatin, and the detail assembly process of flexible ZICs was described later on.

2.4. Materials’ characterization

The morphologies of obtained samples were characterized by SEM (FEI Quanta 200F) and TEM (JEOL JEM-2010). The powder X-ray diffraction patterns were collected on an X-ray diffractometer (Rigaku Ultima IV) with Cu Kα radiation (λ = 0.15406 nm). Nitrogen adsorption–desorption isotherms were measured on a Quanta chrome Autosorbi Q. Specific surface areas were calculated according to the Brunauer-Emmett-Teller equation in a relative pressure range between 0.00 and 1.00P/P_0. Raman spectra were recorded on a Lab RAMHR

confocal Raman system with 532 nm diode laser excitation at room temperature. X-ray photoelectron spectroscopy (XPS) spectra were obtained on Thermo ESCALAB250XI.

2.5. Electrochemical measurements

To prepare carbon cathode, PC or OPC, polyvinylidene fluoride (PVDF) and acetylene black at a mass ratio of 8: 0.5: 1.5 were mixed and dispersed in 1-methy-2-pyrrolidone solvent to form a homogeneous slurry. Subsequently, the slurry was coated on pre-treated carbon cloth, followed by drying at 80 °C for overnight. The mass loading of active materials on the carbon cloth is controlled around 0.8–1.2 mg cm^{-2}. Prior to the assembling, electrodes were soaked with the gelatin/$ZnSO_4$ gel electrolyte. The soaked electrodes were properly cured at room temperature for 1 h, then the two electrodes were combined with the gel electrolyte to afford a sandwich structure, where an appropriate amount of aqueous glutaraldehyde solution was applied to crosslink the gelatin gel. Finally, the assembled hybrid supercapacitors were kept at room temperature to remove excess water in the electrolyte. The overall thickness of the assembled zinc-ion capacitors is about 0.9 mm ± 0.2 mm. Electrochemical performance of these ZICs were evaluated on a CHI 760E and LAND 2001A battery-testing instrument. Specific capacity, energy density and power density of the assembled ZICs were calculated based on the weight of OPC or the total mass of cathode and anode electrode materials.

3. Results and discussion

The schematic illustration for the stepwise synthesis of oxygen functional groups-enriched 3D porous carbon (OPC) is shown in Fig. 1. Firstly, sodium ethoxide with ethanol wrapped in the pores is synthesized using sodium and ethanol as starting materials with the molar ratio of 1:1 via a solvothermal process. From the XRD pattern (Fig. 2a), crystalline sodium ethoxide was found to be the dominant product and the synthetic reaction can be described by the following equation:

$$CH_3CH_2OH + Na \rightarrow CH_3CH_2ONa + \frac{1}{2}H_2\uparrow \quad (1)$$

Furthermore, the free alcohol can be encapsulated into the sodium ethoxide to obtain clathrate-like structure under the conditions of high temperature and high pressure, in which the trapped ethanol is considered as nucleation sites of the carbon sheets [20]. As shown in Fig. 2b and c, scanning electron microscopy (SEM) images reveal that the prepared precursor displays an irregular architecture. In the second step, the violent combustion makes the alkoxide/ethanol precursor decompose to solid carbonized lumps (Fig. S1). The microstructure of the obtained lumps was characterized by SEM as shown in Fig. 2d–f, revealing its three-dimensional macropore structure constructed by numerous particles-covered sheets. The corresponding elemental mapping images of combusted products manifest the uniform distribution of Na and O elements (Fig. 2g). According to the XRD result (Fig. S2), it was found that these particles were ascribed to sodium carbonate resulted from the combustion of sodium ethoxide, which can be removed by water washing to get three-dimensional porous carbon (denoted as PC). Subsequent acid treatment is employed to introduce oxygen-containing functional groups to obtain oxygen-enriched porous carbon (denoted as OPC). The working mechanism of the ZICs is based on reversible ion adsorption/desorption on the cathode of PC or OPC and Zn^{2+} deposition/stripping on the Zn-deposited anode (Fig. 1).

The microstructures of the (porous carbon) PC and oxygen-enriched porous carbon (OPC) are characterized by SEM and TEM. Fig. 2h

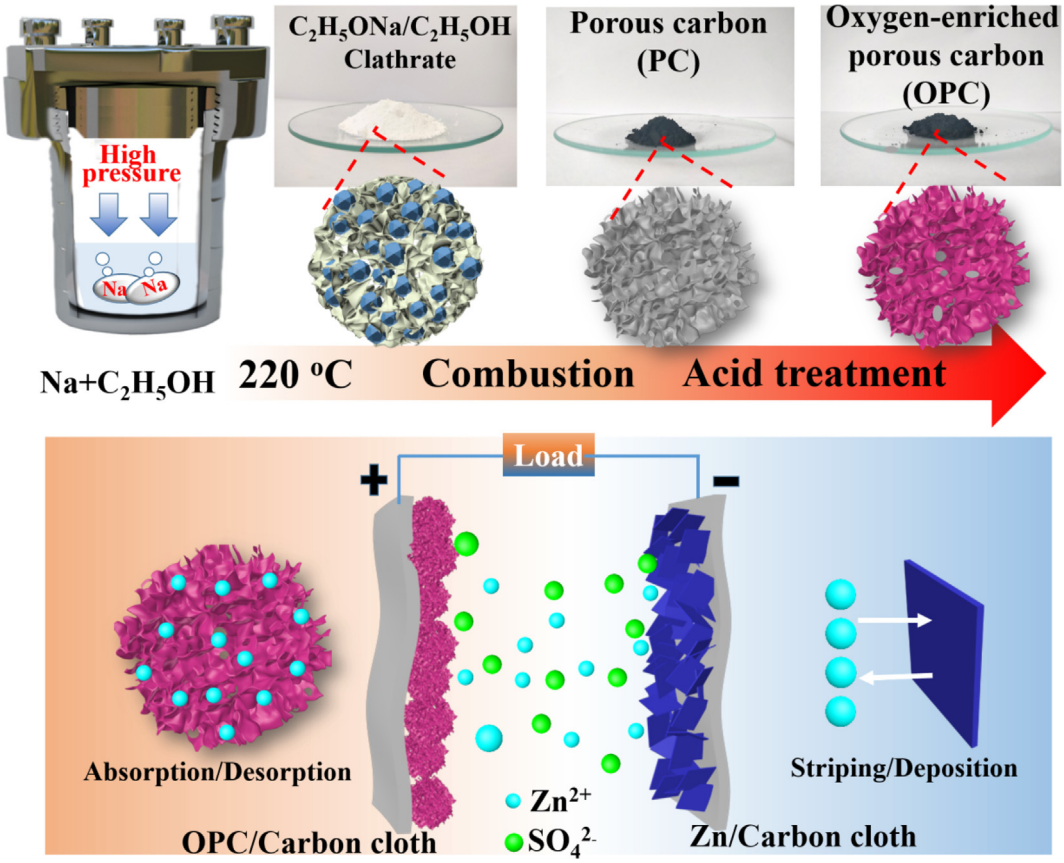

Fig. 1. Schematic illustration for the stepwise preparation of oxygen-enriched 3D porous carbon and the working mechanism of the assembled ZIC based on OPC as the cathode, Zn deposited on pre-treated carbon cloth as anode and gelatin/$ZnSO_4$ hydrogel as the electrolyte.

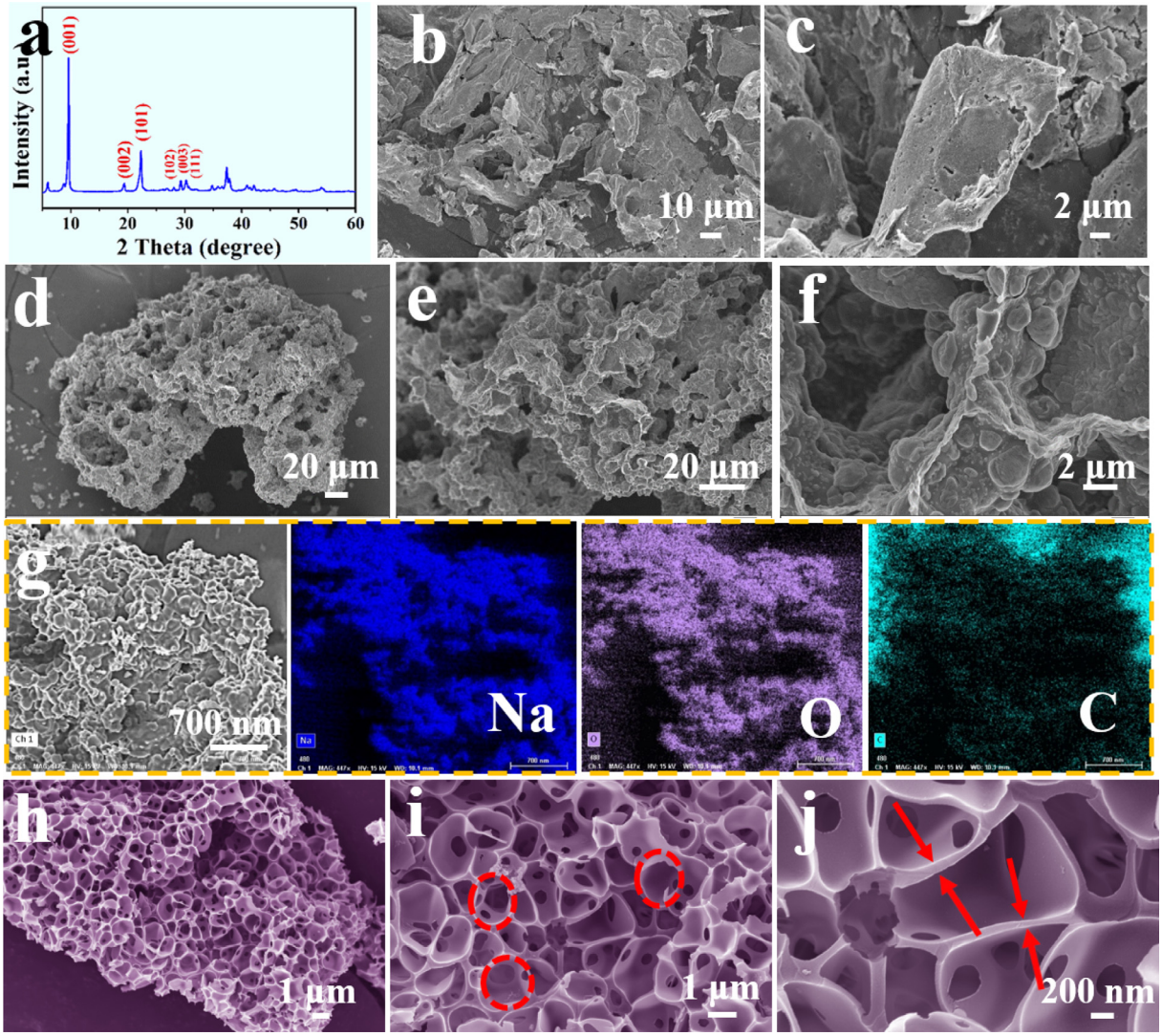

Fig. 2. (a) XRD pattern (b and c) and SEM images of porous carbon precursor; (d-f) SEM images and (g) corresponding elemental mapping images for the combustion products of precursor;(h-j) Low and high magnification SEM images of PC.

reveals that PC owns 3D architecture with interconnected macropores (the pore size distribution is mainly from hundreds of nanometers to several micrometers) separated by carbon walls. These interconnected macropores (marked by the dotted line circle in Fig. 2i) may result from the decomposition of sodium ethoxide in site and can serve as ion-buffering reservoirs as well as ion transport channels [21]. The high magnification SEM image (Fig. 2j) reveals that the nanocarbon is porous with wall thickness of less than 100 nm. The porous nanocarbon structure allows the fast ion diffusion through it. Compared with the recently reported ultrathin carbon [22–24], the thick nanosheets in this work have very tough porous structure, which can be demonstrated by the good structural retention after long circulation.

The overall structure of 3D porous carbon is almost retained after acid treatment (Fig. 3a), demonstrating its robust character. The TEM images of the microstructure of OPC with different magnifications are shown in Fig. 3b and c, from which the highly porous 3D structure is observed, which is consistent with the SEM analysis. The HRTEM image (Fig. 3d and e) of OPC reveals its highly disordered porous carbon structure with a small number of graphite ribbons and displays the continuous distribution of numerous nanopores. The pore structures of PC and OPC are studied by the N_2 sorption experiment. Fig. 3f shows that the adsorption–desorption isotherms of synthesized PC and OPC belongs to the type I isotherm, which indicates a narrow pore size distribution and relatively small external surface of microporous samples with the limiting uptake being governed by the accessible micropore volume rather than by the internal surface area [25]. The pore size distribution of the PC and OPC calculated according to DFT model are shown in Fig. S3. It can be observed that OPC exhibits the higher BET surface of 523 $m^2\ g^{-1}$ than that of PC (315 $m^2\ g^{-1}$), well developed micropores less than 2 nm and higher pore volume of 0.37 $m^3\ g^{-1}$, demonstrating that acid treatment can effectively increase the specific surface area of carbon materials and tune pores structure by reacting carbon materials and residual sodium oxides with concentrated HNO_3 [19].

The powder XRD patterns of PC and OPC are displayed in Fig. 4a, which presents diffraction patterns of a predominantly amorphous carbon. It can be found that after acid treatment, peak at about 23.61° shifts to the lower value of angle and d-spacing increases from 0.3769 nm to 0.409 nm, indicating that intercalation of concentrated HNO_3 increases the interplanar spacing of carbon sheets [26]. Additionally, acid treatment can further remove impurities (denoted as black arrows), especially inorganic compounds (Na_2CO_3 (25–0815) or NaOH (45-0744)) generated from decomposition of sodium salt. In the Raman spectrum (Fig. 4b), two prominent peaks at ~1585.9 cm^{-1} and ~1353 cm^{-1} corresponding to G and D band, should associate with E_{2g} vibration mode in sp^2-bonded graphitic carbons and A_{1g} vibration mode

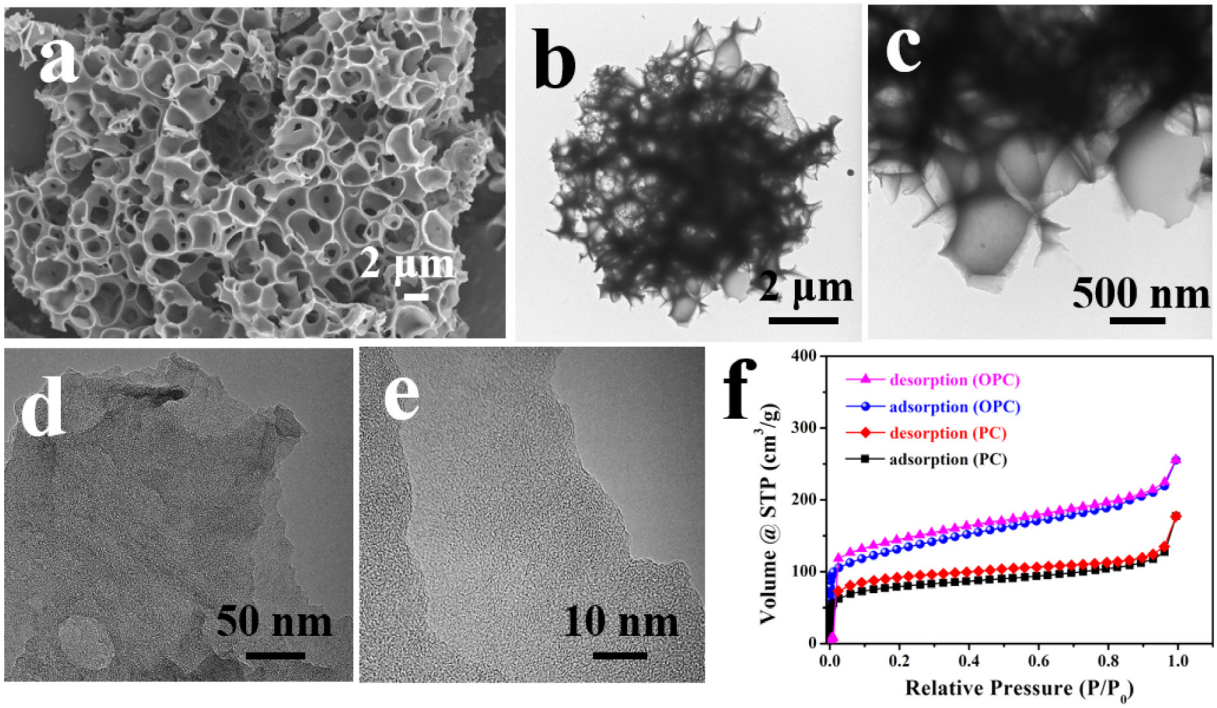

Fig. 3. (a) SEM image of oxygen-enriched porous carbon (OPC), (b and c) Low and high magnification TEM images of OPC, (d and e) High-resolution transmission electron microscopy (HR-TEM) images of OPC. (f) N_2 adsorption and desorption isotherms of OPC and porous carbon (PC).

in defective carbon structure, respectively [27]. Normally, the I_G/I_D is used to evaluate the degree of perfection of carbon materials [6]. From Fig. 4b, OPC show an increased value of I_G/I_D ratio (1.33) than that of PC (1.29), indicating that acid treatment at ambient temperature is able to effectively remove amorphous carbon in PC.

The surface chemistry of the PC and OPC was investigated by FT-IR and X-ray photoelectron spectroscopy (XPS). Fig. S4 shows the FT-IR spectra of PC and OPC, which exhibit similar adsorption peaks. The broad peak at around 3432 cm^{-1} is mainly due to the –OH vibrations. [28] The two peaks at 2922 and 2847 cm^{-1} are attributed to C–H vibrations of CH_2 groups, manifesting that lactonic structures are formed during the combustion and acid-treatment process [29]. Furthermore, the relative intensity of the peak at 605 cm^{-1} corresponding to –OH bending vibrations increased after acid treatment, which suggests the increase of –OH group [30]. Then, the XPS measurement is carried out to further investigate the surface elements and their corresponding

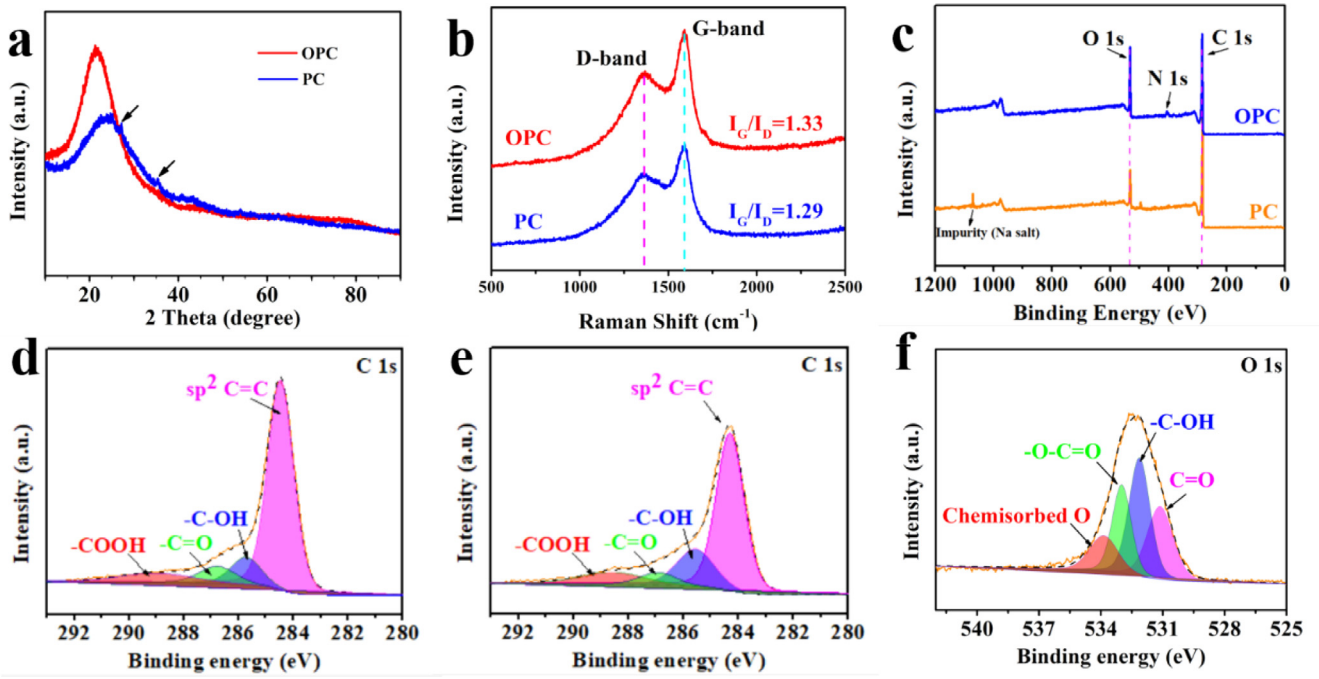

Fig. 4. (a) XRD patterns and (b) Raman spectra of PC and OPC. XPS full spectra of PC and OPC, and core-level XPS spectra: (d) C 1 s for PC; (e and f) C 1 s and O 1 s of OPC. Orange solid curve is the experimental data. The colorful filled curves are deconvoluted peaks. Black dashed curves represent the summation of all the deconvoluted peaks. (For interpretation of the references to colour in this figure legend, the reader is referred to the web version of this article.)

chemical states. In Fig. 4c, elements of C and O are detected in all the samples. The relative oxygen atomic percentages are 11.87% and 19.87% for the PC and OPC, respectively, indicating more oxygen containing groups are introduced on the surface of carbon sheets after immersing PC in concentrated HNO_3. The core-level XPS spectra further disclose the chemical nature of the elements in the materials. From the C1s high resolution XPS spectra of PC (Fig. 4d) and OPC (Fig. 4e), four peaks located at 284.4, 285.6, 286.8 and 288.8 eV can be attributed to the C═C, C–C in aromatic rings, C–O and HO–C═O, respectively. [31,32] For oxygen of OPC, the binding energy around 531 and 532.1 eV should contribute to C═O quinone type groups, C–OH phenol groups and/or C–O–C ether groups, while the peaks at 533 and 534 eV can be ascribed to the –O–C═O ester groups and chemisorbed oxygen (COOH carboxylic groups) and/or water, respectively [33]. It has been proven that oxygen-containing functional groups contribute to pseudocapacitance of electrode materials [34]. The XPS spectrum of O 1 s for PC is supplied in Fig. S5. The result implies that the PC has the same oxygen-containing functional groups as that of OPC and the acid treatment is beneficial for increasing the number of oxygen-containing functional groups.

As anode material, Zn metal was electrodeposited on the surface of carbon cloth to satisfy the requirement of flexibility, and its crystal structure and morphologies were inspected by XRD and SEM. Fig. S6a shows the XRD pattern of Zn@CC, demonstrating its high purity and good crystallinity. The photograph and low-magnification SEM images (Fig.S6b) prove that the prepared Zn metal was homogeneously deposited onto the surface pre-treated carbon cloth. From the high-magnification SEM images (Fig. S6c and d), the interconnected Zn nanosheets are nearly vertically grown on carbon fibers with lateral dimension of 200–500 nm, providing a favorable low resistance pathway for electron transfer and fast ion exchange between electrode and electrolyte. SEM and corresponding elemental mapping image (Fig. S6e) of Zn@CC further manifest the uniform distribution of Zn elements on the surface of carbon fiber. Another important component for solid-state capacitor is the gelatin gel electrolyte whose morphology and viscosity were investigated by SEM and a rotational rheometer. As shown in Fig. S7, the SEM image of the gel electrolyte displayed the wrinkled morphology. For the viscosity measured at room temperature as a function of shear rate, the gel electrolyte with and without glutaraldehyde solution exhibited a viscosity of about 900 Pa·s and 100 Pa·s, respectively (Fig. S8).

The electrochemical performance of the flexible ZIC assembled by Zn@CC as anode and PC or OPC as cathode was investigated using CV and galvanostatic charge/discharge measurements (GCD) measurements. CV curves in Fig. 5a display that the obtained ZIC is able to work in a wide voltage range of 0.2–1.8 V (it has been reported that the oxygen and hydrogen may generate in a wider voltage range [12]). Notably, a pair of humps during both the cathodic and anodic sweeps can be found, manifesting some redox processes contribute to the electrochemical properties of the PC and OPC. It has been proven that the oxygen-containing functional groups carbon materials have pseudocapacitive behavior via electrochemical reactions [35]. This pseudocapacitive behavior has been enhanced after treating PC with concentrated HNO_3, which may be due to the increase of functional groups on the carbon surface. As shown in Fig. 5a, the current density of the OPC is larger than that of PC at the same voltage, manifesting the larger capacity of OPC. The GCD curves in Fig. 5b show discharge capacities of 99.1 mA h g^{-1} and 55.7 mA h g^{-1} at a current density of 0.5 A g^{-1} for OPC and PC, respectively, confirming that acid-treated carbon as cathode can remarkably improve the electrochemical performance of the assembled ZIC.

To better understand the electrochemical kinetics of OPC and PC electrodes in ZICs, the CV measurements are carried out at different scan rates from 5 to 100 mV s^{-1} The CV curves of OPC (Fig. 5c) and PC (Fig. S9) exhibit a deviation from the traditional rectangular, indicating that the charge storage mechanisms are synergistically affected by Zn^{2+} deposition/stripping on the Zn@CC anode and reversible ion adsorption/desorption on the porous carbon cathode [36]. Generally, the current changes against the sweep rate can be described by following equation [37]:

$$i = av^b \tag{2}$$

where, a and b represent the adjustable parameters. When b value is 0.5, the current is controlled by diffusion process, whereas $b = 1$ indicates a capacitive process. As shown in the relationship lines (Fig. 5d) between log (i) (anodic peak current) and log (v), the b-value obtained by the slopes of lines are 0.76 and 0.77 for PC and OPC, respectively, making clear that their electrochemical kinetics are similar and reaction current is influenced by fast capacitive process as well as Zn ion diffusion.[38] In order to quantitatively separate the capacitive and diffusion-controlled contributions, the above formula (2) can be rewritten as

$$i(\mathrm{V}) = k_1 v + k_2 v^{1/2} \tag{3}$$

By calculating k_1 as a function of potential, it is possible to estimate the proportion of current contributed by capacitor-like processes.[39] The separation of the capacitive currents ($k_1 v$, red area) and diffusion currents ($k_2 v^{1/2}$, blue area) for the OPC cathode at a scan rate of 50 mV s^{-1} is shown in Fig. 5e, in which approximately 55.2% of the total current is contributed by the capacitive-controlled process. Furthermore, the contribution of capacitive currents of OPC at other scan rates is calculated and the results are presented in Fig. 5f. It is clear that the contribution of capacitive process increased from 45.6% to 74.5% as the scan rate increased from 30 to 100 mV s^{-1}. The results illuminate that the faradaic reaction induced by the surface oxygen-containing functional groups is the dominating contribution to the capacitance of ZICs based on OPC at the slow scan rate. As shown in Fig. S10. The contribution of capacitive process for PC increased from 42.4% to 64.6% as the scan rate increased from 30 to 100 mV s^{-1}. With the increasing scan rate, the capacitive contribution is improved, resulting in a fast electrochemical kinetic process which is beneficial for achieving superior rate capability of ZICs.

GCD measurement is carried out to obtain capacity, energy density and power density of the assembled ZICs based on OPC or PC as cathode. According to the GCD results (Fig. S11), the ZIC assembled by OPC as cathode delivers a high discharge capacity of 132.7 mA h g^{-1} at a current density of 0.2 A g^{-1}, which is higher than that of PC-based ZIC (82.9 mA h g^{-1}). The rate capability of OPC cathode is shown in Fig. 5g, from which it can be seen that when cycling at current density of 0.2, 0.5, 1.0, 2.0, 3.0 and 4.0 A g^{-1}, the OPC exhibits discharge capacities of 132.7, 99.1, 79, 66, 61 and 54.5 mA h g^{-1}, respectively. The initial inferior rate performance at low current densities may be explained by that the slow diffusion process is dominant as evidenced by Fig. 5f and some irreversible reactions (precipitation-dissolution of $Zn_4SO_4(OH)_6{\cdot}5H_2O$) occur at lower current density [17]. When the current density returns to 0.2 A g^{-1}, the discharge capacity recovers to 121 mA h g^{-1}. The rate performance of PC is shown in Fig. S12, from which it can be seen that when cycling was carried out at current density of 0.2, 0.5, 1.0 and 2.0 A g^{-1}, the OPC exhibited discharge capacities of 132.7, 99.1, 79 and 66 mA h g^{-1}, respectively. The long-term cycling stability of OPC-based ZIC is tested by GCD measurement at a current density of 1 A g^{-1}. After 10,000 cycles, the discharge capacity is 68.4 mA h g^{-1}, which is 87.6% of the capacity in the first cycle. The attenuation of capacity is probably because the irreversible consumption of Zn nanosheets cathode during the long-term as well as the fast charge and discharge processes [40]. As shown in Figs. S13 and S14, the nanosheet morphologies of Zn anode and OPC cathode were well reserved after cycling measurement, evidencing the good structure stability. The specific energy density as a function of power density is given in a Ragone plot, as shown in Fig. 5h. The largest gravimetric energies of ZIC using OPC and PC as electrode material are 82.36 W h kg^{-1} and 44.14 W h kg^{-1} (based on the mass of OPC and

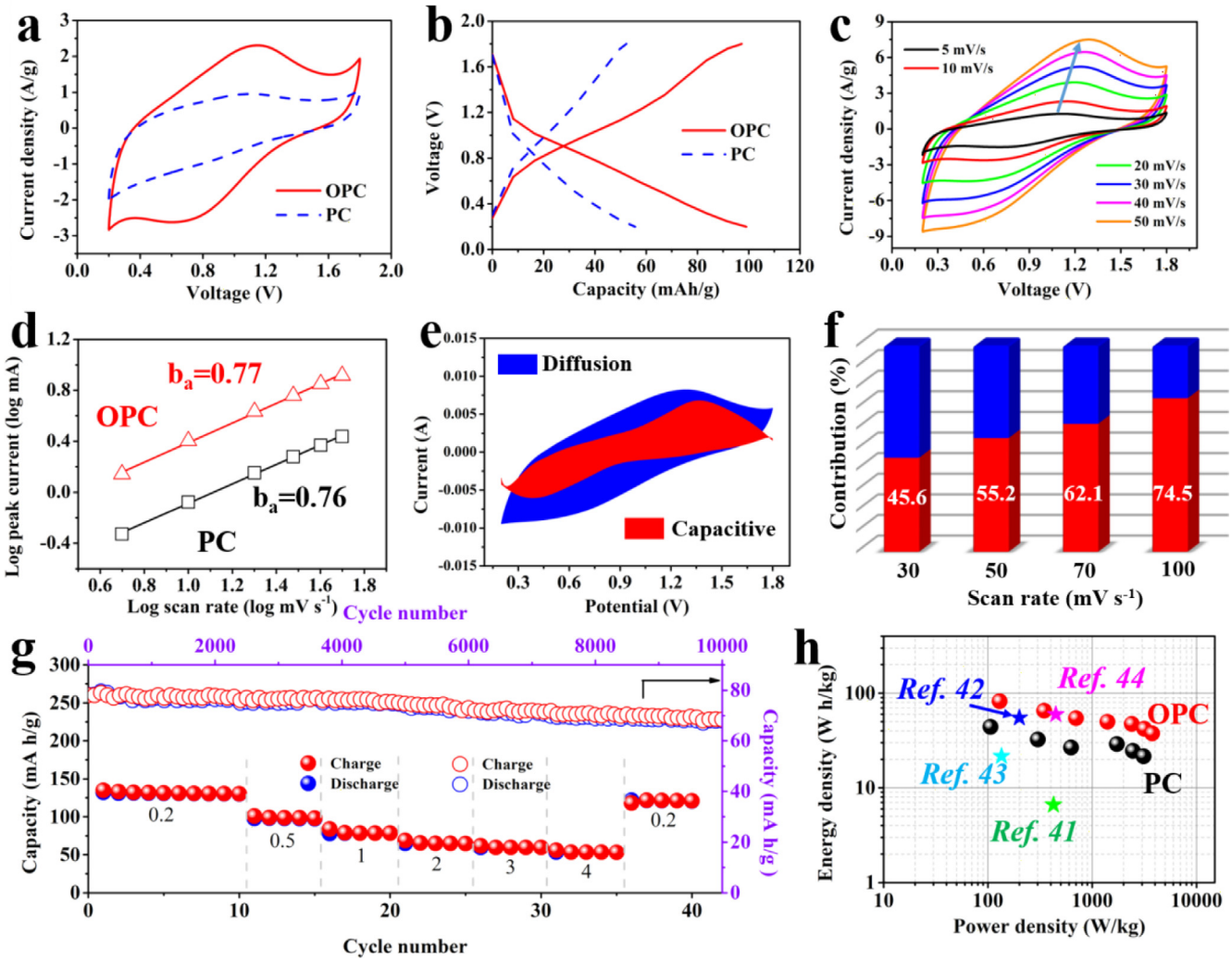

Fig. 5. Electrochemical performances of flexible ZIC assembled by Zn@CC as anode and PC or OPC as cathode. (a) CV curves of PC and OPC at a scan rate of 10 mV s^{-1}. (b) galvanostatic charge/discharge curves of PC and OPC at 0.5 A g^{-1}. (c) CV curves of OPC at various scan rates from 5 − 50 mV s^{-1}. (d) Comparison of *b* values in the anodic scans from 5.0 to 50 mV s^{-1}. (e) Red area represents the capacitive contribution from OPC at a scan rate of 50 mV s^{-1}. (f) The contribution ratio of the capacitive capacities and diffusion-limited capacities at scan rate of 30–100 mV s^{-1}. (g) Rate capability at various rates and cycling stability at a current density of 1.0 A g^{-1} for OPC. (h) Ragone plots of the ZIC using PC or OPC as the cathode. (For interpretation of the references to colour in this figure legend, the reader is referred to the web version of this article.)

PC), respectively. Even at a high power density of 3760 W kg^{-1}, the OPC still exhibits an excellent energy density of 38.6 W h kg^{-1}. Based on the total mass of positive and negative electrodes materials (Fig. S15), the largest gravimetric energies of ZIC using OPC and PC as electrode materials are 30.89 W h kg^{-1} and 17.66 W h kg^{-1}, respectively. These performances are comparable to those of the reported carbon-based flexible hybrid capacitors [41–44].

For assessing the potential application of obtained ZICs for flexible and wearable energy storage, a prototype of solid-state ZIC with working area of 1.5 × 4 cm^2 was bended at 0°, 90° and 180° as well as twisted (Fig. 6a). The corresponding CV curves (Fig. 6b) recorded at 50 mV s^{-1} and GCD curves (Fig. S16a) of the ZICs before and after bending 90°, twisting shows similar capacitive behavior, implying its excellent stability of deformation. Furthermore, the cycling stabilities of the ZICs under different deformation conditions are outstanding as shown in Fig. S16b, which should be attributed to the mechanical stability of carbon cloth-based electrodes and gelatin gel electrolyte. Fig. 6c and d and Fig. S17 displays the CV and GCD curves in regard to the two assembled ZICs devices connected in series and in parallel, respectively. It could be found that the two devices connected in series exhibit a 3.6 V potential limit, which can successfully illuminate ten red LED in parallel (the working potential of a single red LED is 2 V). Meanwhile, the parallel connection of devices displays a ~1.65-fold capacity of a single device, deviating from 2-fold theoretical capacity on account of the mass difference of the two devices [45]. Furthermore, two assembled ZICs connected in series can serve as wristband to power an electronic watch (the working potential is 3 V) and three devices connected in series can charge mobile phone, manifesting a great potential of our assembled ZIC based on OPC cathode for practical applications in wearable and portable electronics.

4. Conclusions

For achieving a high energy and power density as well as flexibility of the portable devices, a novel flexible ZIC is successfully assembled by Zn deposited CC as anode, 3D porous carbon as cathode and glutaraldehyde cross-linked gelatin/$ZnSO_4$ as gel electrolyte. Notably, a facile solvothermal process followed by combustion and acid treatment can be an efficient and effective methodology to synthesize oxygen-enriched porous carbon, whose the unique pore structure endows the fast electrochemical kinetics and oxygen functional groups provide a prominent pseudocapacitance. Meanwhile, Zn nanosheets electrodeposited

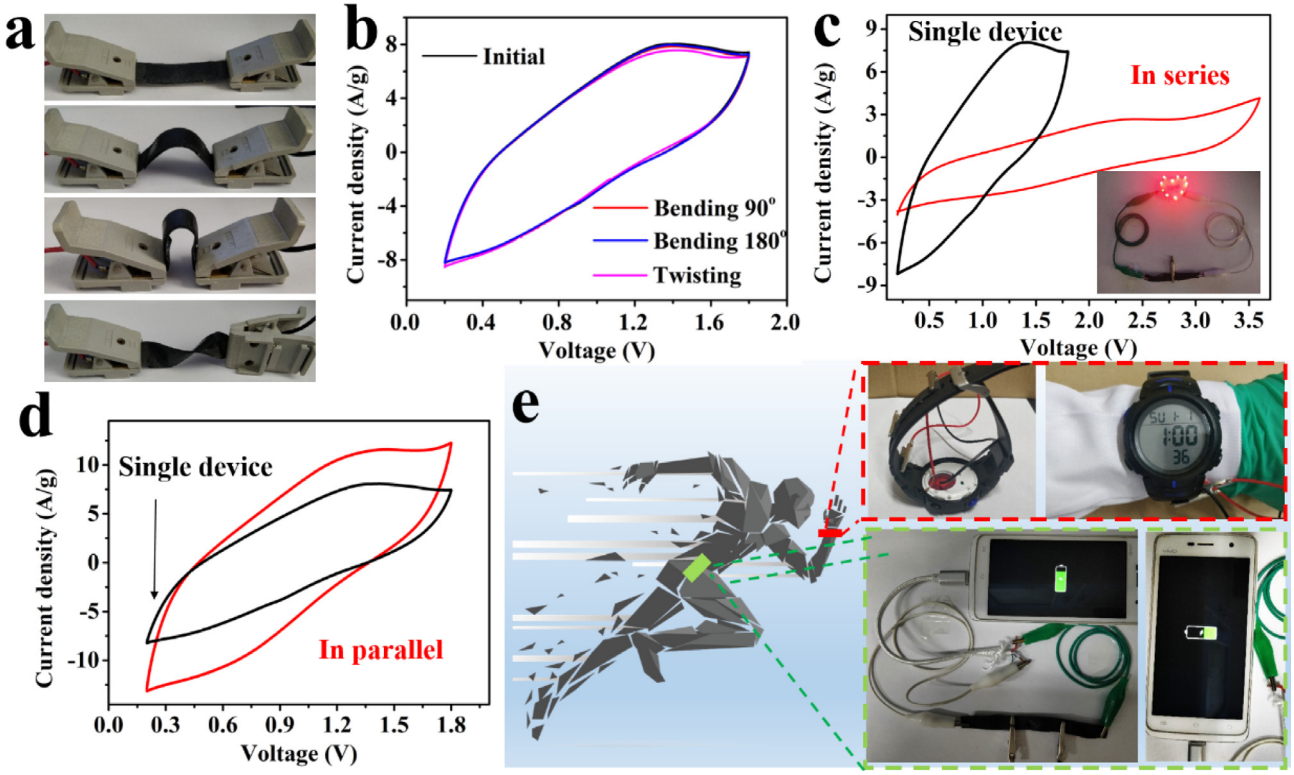

Fig. 6. (a) Photographs of the assembled flexible ZIC at different bending and twisting condition. (b) CV curves of the ZIC recorded at different bending angles (90° and 180°) and twisting condition at a scan rate of 50 mV s^{-1}. CV curves of a single ZIC device and two devices (c) connected in series (the inset is that two ZICs in series could power ten red LEDs in parallel) or (d) in parallel. (e) Photographs of a watch and mobile phone powered by two or three obtained ZICs connected in series. (For interpretation of the references to colour in this figure legend, the reader is referred to the web version of this article.)

on the carbon cloth and gelatin gel electrolyte ensure the excellent mechanical flexibility and fast ion transfer rate. Based on above-mentioned merits, the ZIC based on OPC can deliver the maximal specific capacity of 132.7 mA h g^{-1}, maximal energy density of 82.36 W h kg^{-1} as well as superior cycling stability with 87.6% capacity retention over 10,000 cycles at a current density of 1.0 A g^{-1}. Furthermore, a few as-prepared ZICs connected in series can be utilized to power watch or charge portable devices, manifesting its great potential applications in the flexible and wearable electronics field.

Declaration of Competing Interest

The authors declare that they have no known competing financial interests or personal relationships that could have appeared to influence the work reported in this paper.

Acknowledgements

The authors acknowledge the National Natural Science Foundation of China (21805124) and Natural Science Foundation of Shandong Province (ZR2018BEM020). DW and RKZ acknowledge the Taishan Scholars Program.

Appendix A. Supplementary data

Supplementary data to this article can be found online at https://doi.org/10.1016/j.cej.2020.124161.

References

[1] L. Yao, Q. Wu, P. Zhang, J. Zhang, D. Wang, Y. Li, X. Ren, H. Mi, L. Deng, Z. Zheng, Scalable 2D hierarchical porous carbon nanosheets for flexible supercapacitors with ultrahigh energy density, Adv. Mater. 30 (2018) 1706054.
[2] D.P. Dubal, N.R. Chodankar, D.-H. Kim, P. Gomez-Romero, Towards flexible solid-state supercapacitors for smart and wearable electronics, Chem. Soc. Rev. 47 (2018) 2065–2129.
[3] N.-S. Choi, Z. Chen, S.A. Freunberger, X. Ji, Y.-K. Sun, K. Amine, G. Yushin, L.F. Nazar, J. Cho, P.G. Bruce, Challenges facing lithium batteries and electrical double-layer capacitors, Angew. Chem. Int. Ed. 51 (2012) 9994–10024.
[4] N. Nitta, F. Wu, J.T. Lee, G. Yushin, Li-ion battery materials: present and future, Mater. Today 18 (2015) 252–264.
[5] B. Li, F. Dai, Q. Xiao, L. Yang, J. Shen, C. Zhang, M. Cai, Nitrogen-doped activated carbon for a high energy hybrid supercapacitor, Energy Environ. Sci. 9 (2016) 102–106.
[6] B. Yang, J. Chen, L. Liu, P. Ma, B. Liu, J. Lang, Y. Tang, X.J.E.S.M. Yan, 3D nitrogen-doped framework carbon for high-performance potassium ion hybrid capacitor, Energy Storage Mater. 23 (2019) 522–529.
[7] Y. Ma, H. Chang, M. Zhang, Y. Chen, Graphene-based materials for lithium-ion hybrid supercapacitors, Adv. Mater. 27 (2015) 5296–5308.
[8] J. Ding, H. Wang, Z. Li, K. Cui, D. Karpuzov, X. Tan, A. Kohandehghan, D. Mitlin, Peanut shell hybrid sodium ion capacitor with extreme energy-power rivals lithium ion capacitors, Energy Environ. Sci. 8 (2015) 941–955.
[9] B. Li, F. Dai, Q. Xiao, L. Yang, J. Shen, C. Zhang, M. Cai, Activated carbon from biomass transfer for high-energy density lithium-ion supercapacitors, Adv. Energy Mater. 6 (2016) 1600802.
[10] B. Li, J. Ruan, A. Loh, J. Chai, Y. Chen, C. Tan, X. Ge, T.S.A. Hor, Z. Liu, H. Zhang, Y. Zong, A robust hybrid Zn-battery with ultralong cycle life, Nano Lett. 17 (2017) 156–163.
[11] D. Kundu, B.D. Adams, V. Duffort, S.H. Vajargah, L.F. Nazar, A high-capacity and long-life aqueous rechargeable zinc battery using a metal oxide intercalation cathode, Nat. Energy 1 (2016) 16119.
[12] B.Y. Tang, L.T. Shan, S.Q. Liang, J. Zhou, Issues and opportunities facing aqueous zinc-ion batteries, Energy Environ. Sci. 12 (2019) 3288–3304.
[13] L. Ma, N. Li, C. Long, B. Dong, D. Fang, Z. Liu, Y. Zhao, X. Li, J. Fan, S. Chen, S. Zhang, C. Zhi, Achieving both high voltage and high capacity in aqueous zinc-ion battery for record high energy density, Adv. Funct. Mater. 29 (2019) 1906142.
[14] L. Ma, Y. Zhao, X. Ji, J. Zeng, Q. Yang, Y. Guo, Z. Huang, X. Li, J. Yu, C. Zhi, A usage scenario independent “air chargeable” flexible zinc ion energy storage device, Adv. Energy Mater. 9 (2019) 1900509.
[15] C. Xu, B. Li, H. Du, F. Kang, Energetic zinc ion chemistry: the rechargeable zinc ion battery, Angew. Chem. Int. Ed. 51 (2012) 933–935.
[16] L. Ma, S. Chen, D. Wang, Q. Yang, F. Mo, G. Liang, N. Li, H. Zhang, J.-A. Zapien, C. Zhi, Super-stretchable zinc–sir batteries based on an alkaline-tolerant dual-network hydrogel electrolyte, Adv. Energy Mater. 9 (2019) 1803046.
[17] L. Dong, X. Ma, Y. Li, L. Zhao, W. Liu, J. Cheng, C. Xu, B. Li, Q.-H. Yang, F. Kang,

Extremely safe, high-rate and ultralong-life zinc-ion hybrid supercapacitors, Energy Storage Mater. 13 (2018) 96–102.
[18] L. Dong, W. Yang, W. Yang, Y. Li, W. Wu, G. Wang, Multivalent metal ion hybrid capacitors: a review with a focus on zinc-ion hybrid capacitors, J. Mater. Chem. A 7 (2019) 13810–13832.
[19] Y. Zheng, W. Zhao, D. Jia, L. Cui, J. Liu, Thermally-treated and acid-etched carbon fiber cloth based on pre-oxidized polyacrylonitrile as self-standing and high area-capacitance electrodes for flexible supercapacitors, Chem. Eng. J. 364 (2019) 70–78.
[20] M. Choucair, P. Thordarson, J.A. Stride, Gram-scale production of graphene based on solvothermal synthesis and sonication, Nat. Nanotechnol. 4 (2009) 30–33.
[21] S. Song, F. Ma, G. Wu, D. Ma, W. Geng, J. Wan, Facile self-templating large scale preparation of biomass-derived 3D hierarchical porous carbon for advanced supercapacitors, J. Mater. Chem. A 3 (2015) 18154–18162.
[22] Z. Tang, G. Zhang, H. Zhang, L. Wang, H. Shi, D. Wei, H. Duan, MOF-derived N-doped carbon bubbles on carbon tube arrays for flexible high-rate supercapacitors, Energy Storage Mater. 10 (2018) 75–84.
[23] K. Jayaramulu, D. Dubal, B. Nagar, V. Ranc, O. Tomanec, M. Petr, K. Datta, R. Zboril, P. Gomez-Romero, R.A. Fischer, Ultrathin hierarchical porous carbon nanosheets for high-performance supercapacitors and redox electrolyte energy storage, Adv. Mater. 30 (2018) 1705789.
[24] Q. Wu, L. Yang, X. Wang, Z. Hu, Carbon-based nanocages: a new platform for advanced energy storage and conversion, Adv. Mater. 1904177 (2019).
[25] E. Vunain, D. Kenneth, T. Biswick, Synthesis and characterization of low-cost activated carbon prepared from Malawian baobab fruit shells by H_3PO_4 activation for removal of Cu(II) ions: equilibrium and kinetics studies, Appl. Water Sci. 7 (2017) 4301–4319.
[26] A.K. Sharma, R. Sharma, R. Prajapati, S. Chaudhary, Effect of different acid oxidation on morphology, dispersion and optical band-gap of multi-walled carbon nanotubes, Fullerenes Nanotubes Carbon Nanostruct. 24 (2016) 332–338.
[27] W. Qian, F. Sun, Y. Xu, L. Qiu, C. Liu, S. Wang, F. Yan, Human hair-derived carbon flakes for electrochemical supercapacitors, Energy Environ. Sci. 7 (2014) 379–386.
[28] V. Gómez-Serrano, F. Piriz-Almeida, C.J. Durán-Valle, J. Pastor-Villegas, Formation of oxygen structures by air activation. A study by FT-IR spectroscopy, Carbon 37 (1999) 1517–1528.
[29] Y. Liu, X. Liu, W. Dong, L. Zhang, Q. Kong, W. Wang, Efficient adsorption of sulfamethazine onto modified activated carbon: a plausible adsorption mechanism, Sci. Rep. 7 (2017) 12437.
[30] H. Zhou, C. Liu, J.-C. Wu, M. Liu, D. Zhang, H. Song, X. Zhang, H. Gao, J. Yang, D. Chen, Boosting the electrochemical performance through proton transfer for the Zn-ion hybrid supercapacitor with both ionic liquid and organic electrolytes, J. Mater. Chem. A 7 (2019) 9708–9715.
[31] Y. Song, T. Liu, M. Li, B. Yao, T. Kou, D. Feng, F. Wang, Y. Tong, X.-X. Liu, Y. Li, Engineering of mesoscale pores in balancing mass loading and rate capability of hematite films for electrochemical capacitors, Adv. Energy Mater. 8 (2018) 1801784.
[32] K. Sun, S. Yu, Z. Hu, Z. Li, G. Lei, Q. Xiao, Y. Ding, Oxygen-containing hierarchically porous carbon materials derived from wild jujube pit for high-performance supercapacitor, Electrochim. Acta 231 (2017) 417–428.
[33] D. Hulicova-Jurcakova, M. Seredych, G.Q. Lu, T.J. Bandosz, Combined effect of nitrogen- and oxygen-containing functional groups of microporous activated carbon on its electrochemical performance in supercapacitors, Adv. Funct. Mater. 19 (2009) 438–447.
[34] H. Liu, H. Song, X. Chen, S. Zhang, J. Zhou, Z. Ma, Effects of nitrogen- and oxygen-containing functional groups of activated carbon nanotubes on the electrochemical performance in supercapacitors, J. Power Sour. 285 (2015) 303–309.
[35] V. Ruiz, S. Roldan, I. Villar, C. Blanco, R. Santamaria, Voltage dependence of carbon-based supercapacitors for pseudocapacitance quantification, Electrochim. Acta 95 (2013) 225–229.
[36] G. Sun, H. Yang, G. Zhang, J. Gao, X. Jin, Y. Zhao, L. Jiang, L. Qu, A capacity recoverable zinc-ion micro-supercapacitor, Energy Environ. Sci. 11 (2018) 3367–3374.
[37] Y. Wang, Y. Song, Y. Xia, Electrochemical capacitors: mechanism, materials, systems, characterization and applications, Chem. Soc. Rev. 45 (2016) 5925–5950.
[38] X. Dai, F. Wan, L. Zhang, H. Cao, Z. Niu, Freestanding graphene/VO_2 composite films for highly stable aqueous Zn-ion batteries with superior rate performance, Energy Storage Mater. 17 (2019) 143–150.
[39] C. Xia, J. Guo, Y. Lei, H. Liang, C. Zhao, H.N. Alshareef, Rechargeable aqueous Zinc-ion battery based on porous framework zinc pyrovanadate intercalation cathode, Adv. Mater. 30 (2018) 1705580.
[40] P. Zhang, Y. Li, G. Wang, F. Wang, S. Yang, F. Zhu, X. Zhuang, O.G. Schmidt, X. Feng, Zn-ion hybrid micro-supercapacitors with ultrahigh areal energy density and long-term durability, Adv. Mater. 31 (2019) 1806005.
[41] S.T. Senthilkumar, N. Fu, Y. Liu, Y. Wang, L. Zhou, H. Huang, Flexible fiber hybrid supercapacitor with $NiCo_2O_4$ nanograss@carbon fiber and bio-waste derived high surface area porous carbon, Electrochim. Acta 211 (2016) 411–419.
[42] S. Dong, L. Shen, H. Li, G. Pang, H. Dou, X. Zhang, Flexible sodium-ion pseudocapacitors based on 3D $Na_2Ti_3O_7$ nanosheet arrays/carbon textiles anodes, Adv. Funct. Mater. 26 (2016) 3703–3710.
[43] Y. Liu, Q. Lu, Z. Huang, S. Sun, B. Yu, U. Evariste, G. Jiang, J. Yao, Electrodeposition of Ni-Co-S nanosheet arrays on N-doped porous carbon nanofibers for flexible asymmetric supercapacitors, J. Alloys Compd. 762 (2018) 301–311.
[44] S. Chen, L. Ma, K. Zhang, M. Kamruzzaman, C. Zhi, J.A. Zapien, A flexible solid-state zinc ion hybrid supercapacitor based on co-polymer derived hollow carbon spheres, J. Mater. Chem. A 7 (2019) 7784–7790.
[45] S.J. Patil, D.-W. Lee, Scalable and ascendant synthesis of carbon cloth coated hierarchical core-shell CoMoS@$Co(OH)_2$ for flexible and high-performance supercapacitors, J. Mater. Chem. A 6 (2018) 9592–9603.